AIAA SciTech Forum
4-8 January 2016, San Diego, California, USA
57th AIAA/ASCE/AHS/ASC Structures, Structural Dynamics, and Materials Conference

10.2514/6.2016-0939

Large-Scale Compliance-Minimization and Buckling Topology Optimization of the Undeformed Common Research Model Wing

Ting Wei Chin* and Graeme J. Kennedy†
School of Aerospace Engineering, Georgia Institute of Technology, Atlanta, Georgia

Next-generation additive manufacturing technologies will enable novel, low-weight, high-performance aircraft structures. Topology optimization techniques can be used to obtain unconventional internal aircraft wing structures that can be manufactured using additive methods which depart significantly from conventional rib-spar wing constructions. However, there are significant issues that must be overcome when applying traditional topology optimization techniques to the design of aerospace structures. These challenges include efficiently solving large-scale design problems, and applying buckling criteria within a topology optimization design formulation. In this paper, we seek to address these issues by applying a scalable topology optimization method to the undeformed Common Research Model (uCRM) wing with buckling constraints applied to the skins of the wingbox. The proposed approach uses a multigrid-preconditioned Krylov method to solve the large-scale finite element analysis problem, coupled with a parallel interior-point optimizer to solve the large-scale constrained design optimization problem. This proposed method is applied to two different optimization problems: mass-constrained compliance minimization, and mass-constrained buckling-load maximization. In addition, we apply a segment-wise topology optimization design strategy to the uCRM wingbox.

I. Introduction

Additive manufacturing will enable the construction of unconventional internal wing structures that may offer performance improvements over rib-spar constructions. Topology optimization techniques can be used to design these unconventional structures free from any preconceptions about the structural layout. However, high aspect-ratio wings present computational challenges to conventional density-based topology optimization methods that require a spatially uniform discretization of the problem domain. As a result, conventional topology optimization methods produce large-scale design optimization problems when applied to high aspect-ratio domains, such as aircraft wings.

Industrial applications of topology optimization have primarily focused on component-scale structural design using compliance-based methods [20, 11, 7]. Several authors have presented methods for compliance minimization with either aerodynamic constraints or mass constraints [22, 13]. Due to the low volume fraction of aerospace structures, and their resulting slenderness, buckling and strength are key design requirements.

To design low-weight, high-performance aerospace structures, we develop methods for large-scale topology problems that include buckling, strength and stiffness requirements. To meet the demands of low-volume fraction aerospace structures, we focus on topology optimization methods that are suitable for problems with greater than 10^6 design variables. To successfully apply topology optimization at this scale, we use both a parallel analysis method and a parallel optimization algorithm presented by Kennedy [15]. We focus on two different optimization problems: mass-constrained compliance minimization, and mass-constrained buckling optimization. We apply these methods to the undeformed Common Research Model (uCRM) wing configuration [19] subject to point loads and fixed aerodynamic loads.

The remainder of this paper is structured as follows: In Section II, we give an overview of the literature on structural and large-scale topology optimization. In Section III, we describe the topology parameterization that we use in this work. In Section IV, we present the parallel multigrid method that we use as the preconditioner for the large-scale structural analysis problem. In Section V, we present the formulation of two different optimization problems, as well as a description of the interior point optimizer and the structural and aerodynamic analysis models. In Section VI, we present the compliance minimization, as well as the buckling optimization results that we obtain using the aforementioned methods. In Section VII, we present an alternate segment-based approach to the design of the uCRM structure. Finally, in Section VIII, we present the conclusions from our work.

*Graduate Student
†Assistant Professor, AIAA Member

II. Overview of large-scale topology optimization techniques

Topology optimization techniques are often used in a preliminary design setting to obtain designs without constraints on structural geometry or topology. Aerospace companies have increasingly used topology optimization for preliminary component-scale design of aircraft structures. Airbus employed topology optimization techniques in the redesign of A380 components such as the inboard inner fixed leading edge ribs, inboard outer fixed leading edge ribs and the fuselage door intercostals, leading to weight savings on the order of 10^3 kg per aircraft [20, 11]. Similarly, Bombardier incorporated topology optimization in the design of its passenger jet's wingbox ribs, resulting in a reduction of the weight of the component by 10% [7].

Within academia, some authors have focused on large-scale topology optimization applications. Borrvall and Petersson [5] developed techniques for large-scale topology optimization of 3D elastic continua using regularized density control by using parallel computing techniques to solve problems with up to 663 000 design variables. Amir et al. [2] used an algebraic multigrid method as a preconditioner to solve large 3D compliance topology optimization problems with up to 400 000 design variables. Aage et al. [1] developed a framework using PETSc for compliance-based large-scale topology optimization and applied this framework to a cantilever beam with 27.6 million design variables. More recently, Kennedy [15] used a multigrid-preconditioned Krylov method in conjunction with parallel interior point optimization method to solve a mass constrained compliance minimization with 5.24 million design variables, demonstrating optimization parallelism and scalability.

Other authors have focused on applying topology optimization techniques to multidisciplinary design of full-scale aircraft structures. For example, in one of the first applications of topology-based wing design, Balabanov and Haftka [3] modeled the internal structure of the wing as a ground structure consisting of over 3000 truss elements to determine the number of spars and ribs in the wing. Later, Maute and Allen [22] considered a medium size topology problem, with $O(10^5)$ degrees of freedom, where the internal structure of the wing is modeled by a three-layered plate coupled with aerodynamic loads. More recently, James et al. [13] presented a multidisciplinary framework for performing shape and topology optimization on a flexible wing structure with a total of 71 500 design variables, which showed that concurrent aerostructural optimization of a wing yields a design that achieves a 42% drag reduction compared with a sequentially optimized wing. Dunning et al. [8] presented a multidisciplinary framework that included coupled aerodynamic loads and performed topology optimization using the level-set method. This framework was used to optimize a straight, linearly tapered 3D wing, producing unconventional results compared to traditional spar-rib configurations. Note that in these applications, the number of topology variables is considered to be in the moderate range.

These multidisciplinary applications have used compliance or stiffness-based criteria. Other authors have focused on applying buckling constraints to slender structures loaded in-plane. Neves et al. [23] presented a method to include a buckling criterion within the context of a topology optimization using a linear buckling model. Neves et al. found that during the optimization, low-density regions buckled at artificially low critical loads. Several authors have presented methods to overcome this issue. Neves et al. [23] suggested neglecting the contributions to the geometric stiffness matrix from low density regions. Lindgaard and Dahl [21] found that for linear buckling, different penalization schemes for the stiffness matrix and geometric stiffness matrix alleviated the artificial buckling issues. In addition, Lindgaard and Dahl proposed using one material interpolation scheme for all tangent stiffness matrices as well as the residuals. More recently, Gao and Ma [10] proposed a method where both low-order and high-order artificial buckling modes are identified by comparing the modal strain energy of a low density regions to the total modal strain energy.

Some authors have also included stress constraints within topology optimization. Verbart et al. [33] presented a level set approach for stress-constrained topology optimization. Their approach used consistent sensitivity analysis and a division of stress constraints into different groups. Similarly, Holmberg et al. [12] used a stress constraint clustering approach which, depending on the number of clusters, can be used to vary the control on the local stresses without computing the stresses on every element. In both cases, the methods were applied to 2D problems.

III. Topology optimization parameterization

In this section, we describe the topology design parameterization techniques that are applied to the topology optimization of aircraft wing structures. We use a single material formulation for compliance design problems and a two-thickness formulation for buckling design.

For the compliance-minimization problems, we use a solid-void formulation, where the stiffness-density relations are expressed using either the Solid Isotropic Material with Penalization (SIMP) [4] interpolation or the Rationale Approximation of Material Properties (RAMP) interpolation [30]. Both the SIMP and RAMP formulations can be

expressed as follows:

$$\begin{aligned} \mathbf{C}_j(\mathbf{x}) &= \mathbf{C} w_j(\mathbf{x}), \\ \rho_j(\mathbf{x}) &= \rho \mathbf{x}_j, \end{aligned} \tag{1}$$

where $\mathbf{x} \in \mathbb{R}^N$ are the design variables, $\mathbf{x}_j$ is the j-th component of $\mathbf{x}$, $w_j(\mathbf{x})$ is a design-dependent weight that depends on the type of penalization, and $\mathbf{C}_j(\mathbf{x})$ and $\rho_j(\mathbf{x})$ are the parameterized constitutive matrix and density, respectively, and $\mathbf{C}$ and ρ are the constitutive matrix and density of the full material. For SIMP penalization, the design-dependent weight function $w_j(\mathbf{x})$ is

$$w_j(\mathbf{x}) = \mathbf{x}_j^p,$$

where p is the SIMP exponent, whereas for RAMP penalization, the design-dependent weight function takes the form:

$$w_j(\mathbf{x}) = \frac{\mathbf{x}_j}{1 + p(1 - \mathbf{x}_j)},$$

where p is the RAMP parameter.

Each element in the domain is associated with a single design variable which is restricted to the range $\mathbf{x}_j \in [\varepsilon, 1]$, where ε is a small but finite value. A solution of the topology optimization problem ideally satisfies the condition that the design variables are nearly discrete such that $\mathbf{x}_j \in \{\varepsilon, 1\}$. The SIMP or RAMP penalization force the design to a nearly discrete solution by favoring design points that are either solid or void material with $\mathbf{x}_j \in \{\varepsilon, 1\}$, rather than intermediate designs. At intermediate points, the SIMP or RAMP scheme imposes a penalization that reduces the stiffness-to-mass ratio, making the intermediate design less-favorable compared to the stiffness-to-mass ratio of a discrete design.

For compliance-minimization, we use a RAMP penalization scheme. This is chosen instead of SIMP penalization due to the non-zero derivative of the penalization with respect to the design variable at $\mathbf{x}_j = 0$. This property often forces SIMP-based optimizations to stall when $\mathbf{x}_j \approx \varepsilon$. For the results shown below, the values of ε and p are chosen to be 10^{-3} and $p = 5$, respectively.

For the buckling design problems described below, we modify the parameterization (1) to account for a selection between two material thicknesses values given by t_0 and t_1, where $t_0 < t_1$. In this case, the constitutive parameterization (1) is modified to interpolate between the discrete thicknesses t_0 and t_1 as follows:

$$\begin{aligned} \mathbf{t}_j(\mathbf{x}) &= t_0 + (t_1 - t_0)\frac{\mathbf{x}_j}{1 + p(1 - \mathbf{x}_j)}, \\ \rho_j(\mathbf{x}) &= \rho \mathbf{x}_j, \end{aligned} \tag{2}$$

where $\mathbf{x} \in [\varepsilon, 1]^N$ and p is the RAMP-penalization factor. In this formulation $\mathbf{x}_j \approx \varepsilon$ corresponds to the smaller thickness, t_0, while $\mathbf{x}_j = 1$, corresponds to the larger thickness t_1. Similarly to the compliance-minimization case, the values of ε and p are chosen to be 10^{-3} and $p = 3$, respectively.

The topology optimization parameterizations shown above exhibit mesh-dependence and checkerboard instabilities that are common to many topology optimization methods. To overcome these issues, we apply a spatial filter that distributes the stiffness contribution from one design variable spatially across several adjacent elements. This spatial filter is based on the work of Bruns and Tortorelli [6] and written as follows:

$$\hat{\mathbf{x}}_i = \frac{1}{\mathbf{s}_i} \sum_{j \in I_i} (r_0 - \mathbf{r}_{ij}) \mathbf{x}_j, \tag{3}$$

where $\hat{\mathbf{x}}_i$ are the filtered design variables. The conic spatial filter of length r_0 uses the spatial distance, $\mathbf{r}_{ij}$ between the centroids of elements i and j. For each element, the filter uses information from adjacent elements given by the set of indices I_i for $i = 1, \ldots, N$. These sets are defined as follows:

$$I_i = \{ j \in \mathbb{N} \mid \mathbf{r}_{ij} < r_0 \}.$$

Finally, the filter is normalized such that the weights on adjacent design variables do not exceed unity using the scalar quantity:

$$\mathbf{s}_i = \sum_{j \in I_i} (r_0 - \mathbf{r}_{ij}).$$

The filter smooths the local effect of a design variable over adjacent elements. In all the penalization calculations (1) and (2), the filtered variables replace the use of the direct variables.

IV. Parallel solution of large-scale linear systems

In this work, we solve the large linear system of governing equations arising from the finite-element discretization of the wing structure at each optimization iteration. Due to the size of the finite-element mesh, it is not practical to solve this linear system using serial methods. Instead, we use a parallel multigrid algorithm that has been successfully applied to large-scale multimaterial optimization problems [15]. Multigrid algorithms have also been applied by other researchers to large-scale topology optimization problems [2, 1]. For this work, we use a geometric multigrid-preconditioned Krylov subspace method to solve the finite-element governing equations. Using multigrid as a preconditioner allows for both algorithmic and parallel scalability. Due to the ease of implementation within the existing finite element analysis and design framework [17], we have chosen geometric multigrid instead of algebraic multigrid.

Geometric multigrid is a multilevel iterative method that operates on a set of meshes with different levels of refinement [35, 26]. These meshes are linked through the prolongation and restriction operators, which transfer the solution and residual between mesh levels. At each level that is not the coarsest mesh, a smoothing operation is carried out through a simple iterative method such as Symmetric Successive Over-Relaxation (SSOR) to attenuate the high frequency solution error. At the coarsest mesh, a coarse grid correction is carried out by solving the relatively small linear system directly, eliminating the lowest frequency errors. Within this work, we take advantage of the efficient parallel direct solution method presented by Kennedy and Martins [17]. This direct solution method uses a Schur-complement based factorization that scales well with the number of processors. Since the direct solution method is applied only on the coarsest mesh, the size of the linear system is relatively small and the direct computation can be carried out efficiently. Using the multigrid algorithm as the preconditioner, we can solve the large linear system using FGMRES(80) [25, 27]. A detailed description of the implementation of the multigrid algorithm is contained in Kennedy [15].

V. Large-scale parallel topology optimization framework

In this section, we present the components of our topology optimization framework, as well as the uCRM wingbox used in this study.

A. Interior-Point Method

We use an interior-point method, called ParOpt [15], to solve the large-scale design optimization problems within this work. Interior-point methods are well-established robust optimization algorithms that have been applied to a wide range of problems [34, 9]. To achieve good parallel performance, ParOpt stores the design variables, gradient vectors, and Jacobian matrices in a distributed format. ParOpt takes special advantage of multimaterial parameterizations that employ element-based design variables that are aligned with the domain decomposition of the underlying finite-element problem [17]. This element-based scheme, and the structure of the sparse constraints, enables the efficient implementation of a parallel interior-point method for problems with millions of design variables.

B. Aerodynamic Loading

In this work we prescribe a constant load that acts on the structural mesh, neglecting the aeroelastic coupling between the aerodynamic loads and structural deformation. The fixed aerodynamic loads on the structural mesh are determined by TriPan [18]. TriPan is an unstructured three-dimensional panel method that can model the aerodynamics of inviscid, external lifting flows governed by the Prandtl–Glauert equation, using constant source and doublet singularity elements distributed over the lifting surface. Using TriPan, we determine the aerodynamic loading on the wing for certain flight conditions, which is used as a fixed aerodynamic loading during the optimization. In this case, the fixed aerodynamic loading was determined at 1g cruise condition.

C. uCRM Structural Mesh

The Common Research Model (CRM) is a representative aircraft geometry for a modern, long-range, transonic aircraft first developed by Vassberg et al. [32] for the purpose of validating the drag prediction capabilities of CFD codes. The geometry of the CRM has a built-in 1g cruise shape, which is not well-suited for aerostructural analysis or design. To address this issue, Kenway et al. [19] proposed the undeformed CRM (uCRM) geometry, where the authors used an inverse design method to remove the built-in 1g-deflection of the original CRM. Kenway et al. [19] further verified that the uCRM wing, shown in Figure 1, is a viable model for aerostructural analysis and design. There are two variants to the uCRM configuration: the uCRM-9, which has an aspect ratio of 9, and the uCRM-13.5, which has an aspect ratio of 13.5. The difference in the planform of the wing is shown in 2. These uCRM geometries serve as our baseline design configuration.

The finite-element structural mesh generated for the topology optimization problem consists of eight-noded, hexahedral elements that fill the entire design domain of the uCRM wing. Both wingbox volume structures are discretized into 136 elements chord-wise, 312 elements span-wise and 8 elements through the thickness, with a total of 339 456 elements in both structural meshes. Figure 2 shows the planform of the aerodynamic surface. Figures 3 shows the two wingboxes that are generated from the aerodynamic surfaces. Note that the aspect ratio of the two wingboxes are larger than their corresponding outer-mold line.

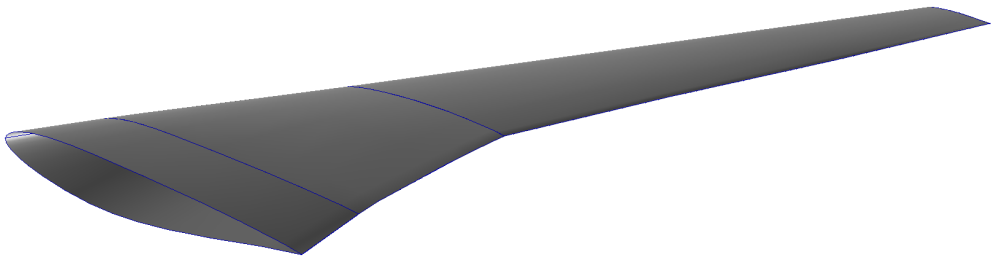

Figure 1: Surface mesh of the uCRM-9 wing

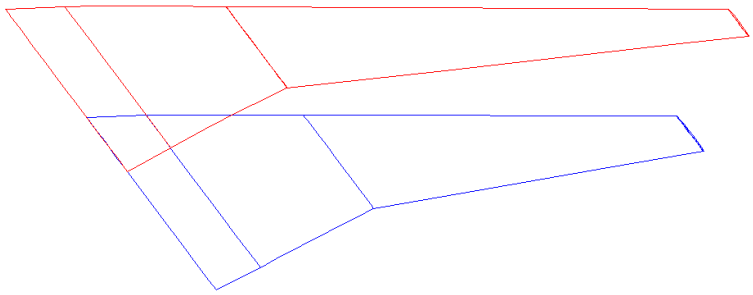

Figure 2: Comparison in the planform between uCRM-9 (blue) and uCRM-13.5 (red)

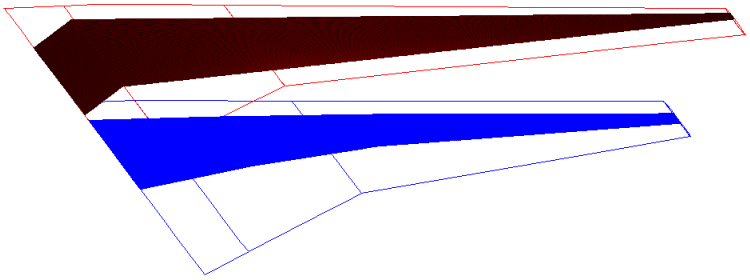

Figure 3: uCRM aerodynamic surface with uCRM-9 (red) and uCRM-13.5 (blue) wingbox

1. uCRM Wing Geometry and Material Properties

The dimension of the baseline uCRM-9 and uCRM-13.5 wing configurations are shown in Figure 4. The uCRM-9 has a semi-span of 29.4 m and the full scale uCRM-13.5 has a semi-span of 36.0 m. However, the wingbox for the uCRM-13.5 is at 10% scale, which results in a scaled semi-span of 3.6 m. The loading for the uCRM-9 and uCRM-13.5 are different. For the uCRM-9 wing, the loads are static aerodynamic loads determined by TriPan as described in Section B. For the 10% scale uCRM-13.5, the loading condition is a single point load at the tip of the wing.

D. Problem Formulations

In this work, we apply the large-scale topology optimization methodology described above to two different design problems: mass-constrained buckling optimization and mass-constrained compliance minimization.

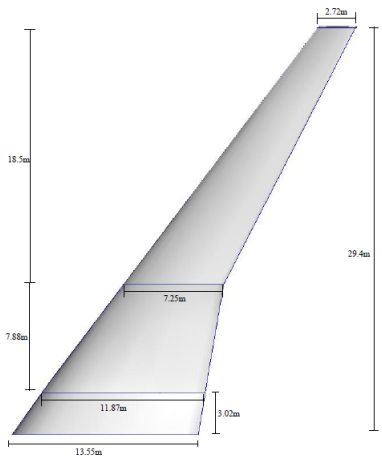

Figure 4: Dimension of the uCRM-9 wing

E (GPa)	70
Density(kg/m^3)	2700
Poisson Ratio	0.3

Table 1: Material properties used in topology optimization

1. Mass-Constrained Compliance Minimization Topology Optimization

The mass-constrained compliance minimization problem is formulated as follows:

$$\begin{aligned} \text{minimize} \quad & c(\mathbf{x}) = \tfrac{1}{2}\mathbf{u}^{\mathbf{T}}\mathbf{f} \\ \text{with respect to} \quad & \mathbf{x} \\ \text{such that} \quad & \mathbf{x}_l \leq \mathbf{x} \leq \mathbf{x}_u \\ & \mathbf{c_s}(\mathbf{x}) = m_{\text{fixed}} - m(\mathbf{x}) \geq 0 \\ \text{governed by} \quad & \mathbf{K}(\mathbf{x})\mathbf{u} = \mathbf{f} \end{aligned} \tag{4}$$

where $c(\mathbf{x})$ is the compliance of the structure, $\mathbf{u}$ are the state variables, and $\mathbf{x}$ are the design variables. In addition, the mass of the structure $m(\mathbf{x})$ is subjected to a scalar fixed-mass constraint $m_{\text{fixed}} = f_V V \rho_{\max}$, where f_V is the volume fraction, fixed at 40%, and V is the volume occupied by the mesh.

E. Mass-Constrained Buckling Topology Optimization

The mass-constrained buckling problem requires the solution of the following eigenvalue problem:

$$\left[\mathbf{K}(\mathbf{x}) + \lambda \mathbf{G}(\mathbf{x}, \mathbf{u}_{\text{p}})\right] \mathbf{u} = \mathbf{0} \tag{5}$$

where $\mathbf{K}(\mathbf{x})$ is the stiffness matrix, $\mathbf{G}(\mathbf{x}, \mathbf{u}_{\text{p}})$ is the geometric stiffness matrix, λ is the eigenvalue, $\mathbf{u}$ is the eigenvector, $\mathbf{u}_{\text{p}}$ is the load path, and $\mathbf{x}$ are the design variables. The load path $\mathbf{u}_{\text{p}}$ is obtained from the solution to the auxiliary linear problem $\mathbf{K}(\mathbf{x})\mathbf{u}_{\text{p}} = \mathbf{f}$.

To optimize the structure for buckling, the minimum eigenvalue of (5) is maximized. However, eigenvalue cross-over is of concern when using this type of design formulation [28]. Cross-over occurs when the mode associated with the minimum eigenvalue changes due to a change in the design variables. This produces a local discontinuity in the slope of the gradient of the eigenvalue. To overcome this issue, we use an aggregation technique that aggregates the lowest n eigenvalues, where n is a chosen parameter. The mass-constrained buckling problem is formulated as follows:

$$\begin{aligned} \text{maximize} \quad & \mathbf{c}_{\text{KS}}(\lambda_j(\mathbf{x})) \quad j = 1, \ldots, n \\ \text{with respect to} \quad & \mathbf{x} \\ \text{such that} \quad & \mathbf{x}_l \leq \mathbf{x} \leq \mathbf{x}_u \\ & \mathbf{c_s}(\mathbf{x}) = m_{\text{fixed}} - m(\mathbf{x}) \geq 0 \\ \text{governed by} \quad & \mathbf{K}(\mathbf{x})\mathbf{u_p} = \mathbf{f} \\ & \left[\mathbf{K}(\mathbf{x}) + \lambda \mathbf{G}(\mathbf{x}, \mathbf{u}_{\text{p}})\right] \mathbf{u} = \mathbf{0} \end{aligned} \tag{6}$$

where $\mathbf{c}_{\text{KS}}$ is the KS aggregation, $m(\mathbf{x})$ is the mass of the structure, $\mathbf{u}$ is an eigenvector, and $\mathbf{x}$ are the design variables. We set m_{fixed} to be the mass due to the average of the two candidate thicknesses. The constraints are aggregated using the aggregation methods presented by Kennedy and Hicken [16] and Kennedy [14].

To handle multiple load cases, we use a min-max formulation that employs a bound-variable, β [31, 24]. This formulation enables the optimization of the wing skin structure subject to both compressive and shear loads. The resulting design optimization problem can be written as follows:

$$\begin{aligned}
\text{min} \quad & -\beta \\
\text{with respect to} \quad & \mathbf{x}, \beta \\
\text{such that} \quad & \mathbf{x}_l \leq \mathbf{x} \leq \mathbf{x}_u \\
& \mathbf{c_s}(\mathbf{x}) = m_{\text{fixed}} - m(\mathbf{x}) \geq 0 \\
& \beta \leq \mathbf{c}_{\text{KS}}(\lambda_j^{\text{comp}}(\mathbf{x})) \\
& \beta \leq \mathbf{c}_{\text{KS}}(\lambda_j^{\text{shear}}(\mathbf{x})) \\
\text{governed by} \quad & \mathbf{K}(\mathbf{x})\mathbf{u_p} = \mathbf{f} \\
& \left[\mathbf{K}(\mathbf{x}) + \lambda \mathbf{G}(\mathbf{x}, \mathbf{u}_{\text{p}})\right] \mathbf{u} = \mathbf{0}
\end{aligned} \tag{7}$$

Lastly, we include stress constraints within the buckling optimization by extending (7) as shown below:

$$\begin{aligned}
\text{min} \quad & -\beta \\
\text{with respect to} \quad & \mathbf{x}, \beta \\
\text{such that} \quad & \mathbf{x}_l \leq \mathbf{x} \leq \mathbf{x}_u \\
& \mathbf{c_s}(\mathbf{x}) = m_{\text{fixed}} - m(\mathbf{x}) \geq 0 \\
& \beta \leq \mathbf{c}_{\text{KS}}(\lambda_j^{\text{comp}}(\mathbf{x})) \\
& \beta \leq \mathbf{c}_{\text{KS}}(\lambda_j^{\text{shear}}(\mathbf{x})) \\
& \mathbf{c}_{\text{KS}}(\frac{\sigma(\mathbf{x}_j)}{\sigma_{\text{VM}}}; \mathbf{u}_{\text{f}}; \rho) \leq 1 \\
\text{governed by} \quad & \mathbf{K}(\mathbf{x})\mathbf{u_p} = \mathbf{f} \\
& \left[\mathbf{K}(\mathbf{x}) + \lambda \mathbf{G}(\mathbf{x}, \mathbf{u}_{\text{p}})\right] \mathbf{u} = \mathbf{0} \\
& \mathbf{K}(\mathbf{x})\mathbf{u}_{\text{f}} = \mathbf{f}
\end{aligned} \tag{8}$$

where $\sigma(\mathbf{x}_j)$ is the stress at $\mathbf{x}_j$, σ_{VM} is the von-Mises stress of the structure, ρ is the density, $\mathbf{u}_{\text{f}}$ are the state variables. As shown in the above optimization problem formulations (4), (6), (7) and (8), the design variables $\mathbf{x}$ are subject to both lower and upper bounds on their values which are $\mathbf{x}_l = 10^{-3}$, and $\mathbf{x}_u = 1$, respectively.

While we work with the volume mesh of the wing in the case of compliance-minimization, buckling in aerospace structures primarily occurs in the skin of the wingbox. Therefore, we use a shell model of the wing surface with two different geometries: a flat plate model and a segment of the upper skin of the uCRM-13.5 shown in Figure 5. Also shown in Figure 5 is the curvature of the uCRM skin mesh.

The buckling optimization of these 2D domains involves a selection between two candidate thickness as illustrated in Table 2. Both candidates are composed of the same material, whose properties are listed in Table 1.

Thickness	(mm)
t_0	2.0
t_1	8.0

Table 2: Candidate thickness used in topology optimization

To impose buckling loads on the flat plate and the uCRM skin, we use displacement boundary conditions on the edges of the mesh, instead of applying forces, to obtain either a pure compressive loading or a pure shear loading. These boundary conditions are illustrated in Figure 6 and Figure 7, respectively.

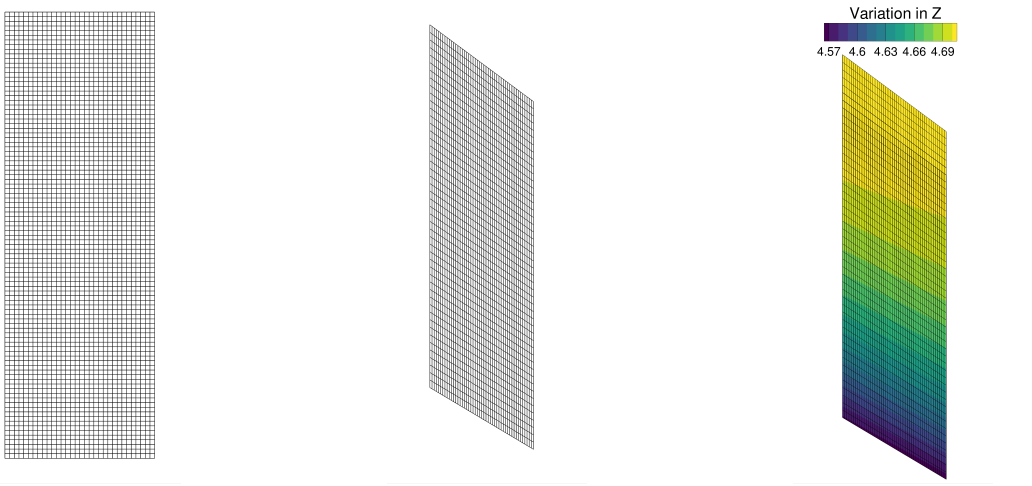

(a) 33×97 mesh (b) 49×49 mesh (c) Curved uCRM skin mesh

Figure 5: Meshes used for the buckling optimization problems

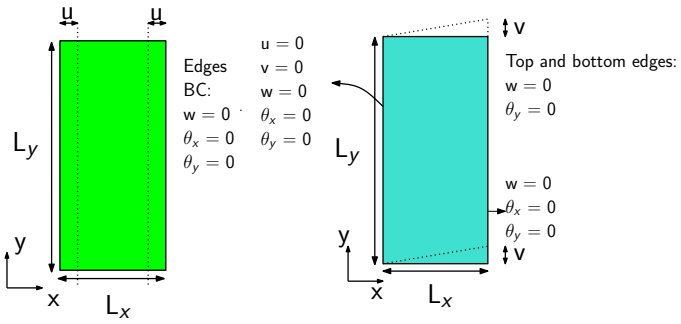

(a) Pure compression (b) Pure shear

Figure 6: Flat plate under imposed buckling displacement conditions

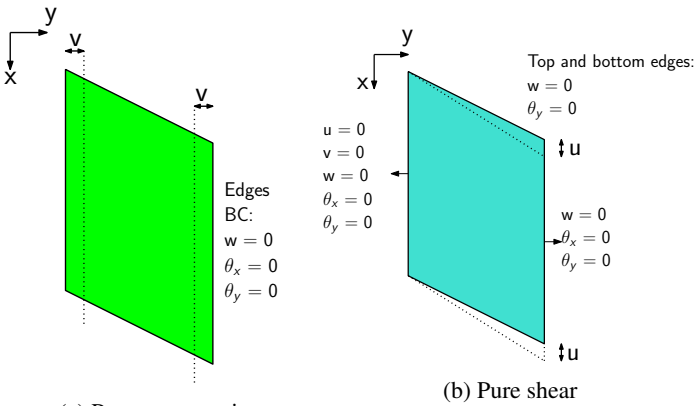

(a) Pure compression (b) Pure shear

Figure 7: uCRM-13.5 skin under buckling displacement conditions

For the stress-constrained load case, we applied a pressure loading on the surface along the z-axis such that the stress constraint is active.

VI. Results

In this section, we present the results from the mass-constrained compliance minimization and mass-constrained buckling optimization problems. We solved these optimization problems using design variable parameterization as presented in Section III, where the different formulation for compliance minimization as well as buckling optimization are presented. All results utilize the spatial filter (3), to alleviate any numerical instabilities or checkerboard patterns [29].

A. uCRM-9 and uCRM-13.5 Wingbox Designs

Figure 8 shows the optimized design for uCRM-9 wingbox under static aerodynamic load, while Figure 9 shows the optimized design for the 10% scale uCRM-13.5 wingbox subjected to a point load at the tip.

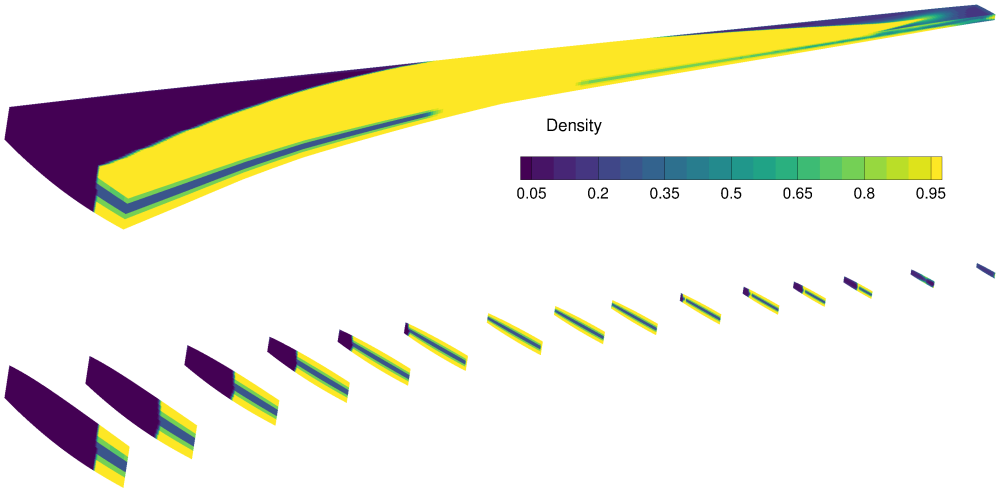

Figure 8: uCRM-9 wingbox optimized for static aerodynamic loading

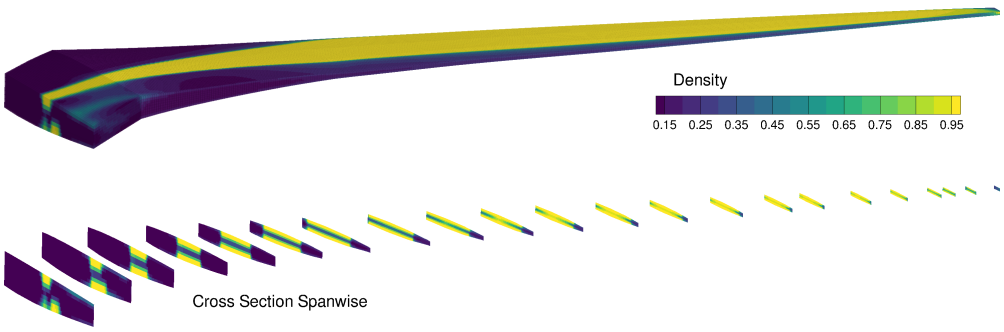

Figure 9: uCRM-13.5 wingbox optimized for tip point loading

The results illustrate the effect of the loading on the final optimized designs. For the design under static aerodynamic loading, most of the material distribution is placed inboard of the wing, given that the loading on the surface is the largest at the root. On the other hand, the optimized uCRM-13.5 design has more material placed near the tip of the wing due to the location of the point load. In both cases, the optimized wingbox designs are not discrete 0-1 solutions. The through-thickness distribution of material in both wingboxes mimics a composite structure. The internal intermediate stiffness material acts in a similar manner to a soft-core with the top and bottom surfaces acting as stiffer face-sheets. This configuration maximizes the bending stiffness of the wing for a given fixed mass.

B. Optimized Design of Flat Plate and uCRM-13.5 Skin

Next, we consider the results from buckling optimization of the wingbox skin. The buckling optimization formulation (7) includes an unspecified number of eigenvalues within the KS aggregation function. To ensure that the design

is not sensitive to the number of eigenvalues, we first investigate how the optimized design changes as the number of aggregated eigenvalues increases.

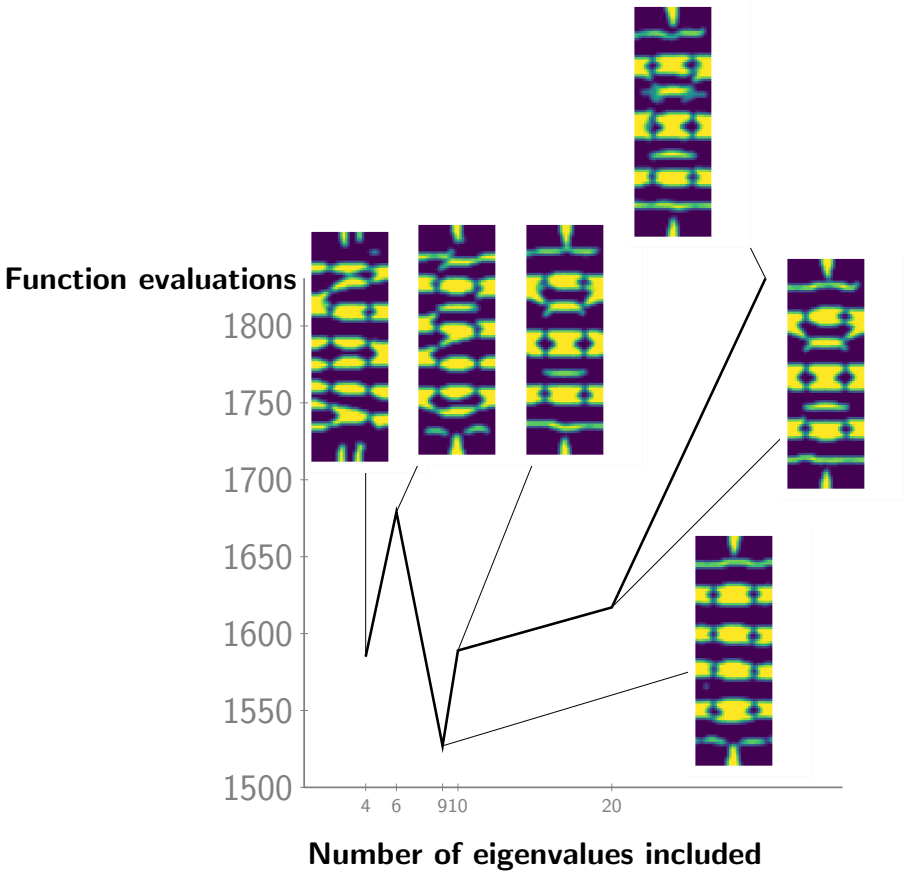

Figure 10: Design changes drastically for less than 10 eigenvalues included

Figure 10 shows the number of function evaluations required for the optimization and the final designs obtained as the number of aggregated eigenvalues increases. For designs with less than ten eigenvalues, the number of axial members varies. Once the number of aggregated eigenvalues exceeds ten, the number and shape of the members in the optimized design remains relatively fixed. Furthermore, increasing the number of eigenvalues beyond ten results in a greater number of function evaluations required to obtain the optimized design. Therefore, the buckling optimization problems presented here, both for the flat plate as well as the uCRM skin, include the ten lowest eigenvalues.

Figure 11 shows the optimized design for the flat plate subjected to both buckling and shear displacement boundary conditions, as well as the buckling mode for the optimized design. Since the mass constraint fixes the total plate mass at the average of the two candidate thicknesses, the final design consists of equal areas of both candidate thicknesses. Furthermore, the thicker candidate material is placed parallel to the compressive load.

Figure 12 shows the optimized design for the uCRM skin segment. The skin segment is extracted from the top skin of the uCRM-13.5 wingbox as shown in Figure 13 and Figure 14. The skin segment is subjected to both buckling and shear displacement boundary conditions. Due to the geometric skew of the skin and the curvature of the segment, the optimized design is different from the previous flat plate design.

Lastly, Figure 15 shows the results for buckling optimization with stress constraints for the flat plate and uCRM skin segment. Due to the stress constraint which smooths out any stress concentration, we see different thickness distribution compared to Figures 11 and 12.

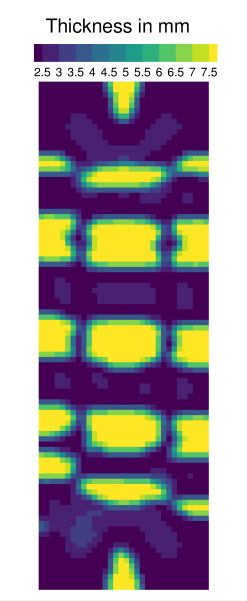

(a) Optimized design obtained after 500 iterations

(b) First buckling mode of optimized design

Figure 11: Optimized design of flat plate and its first buckling mode

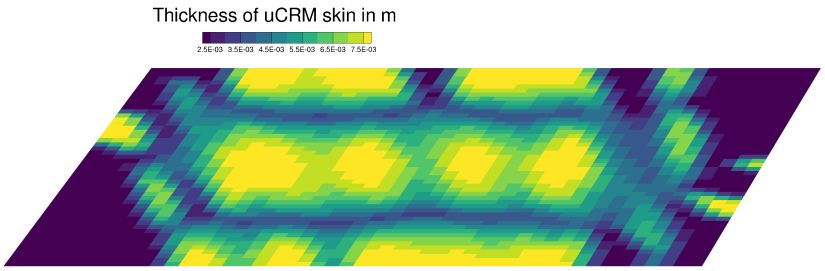

Figure 12: Optimized design of uCRM skin

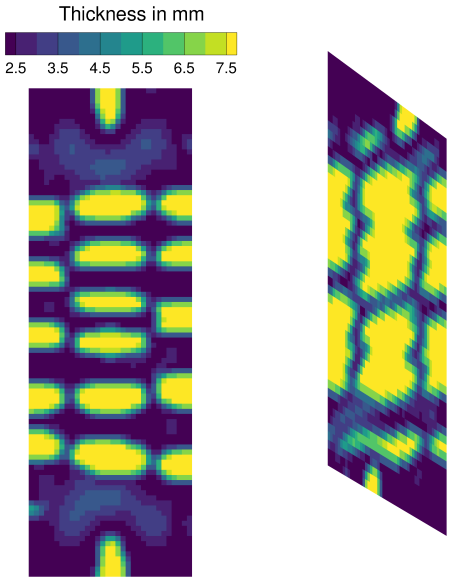

Figure 15: Optimized design with stress constraints of flat plate and uCRM skin segment, respectively.

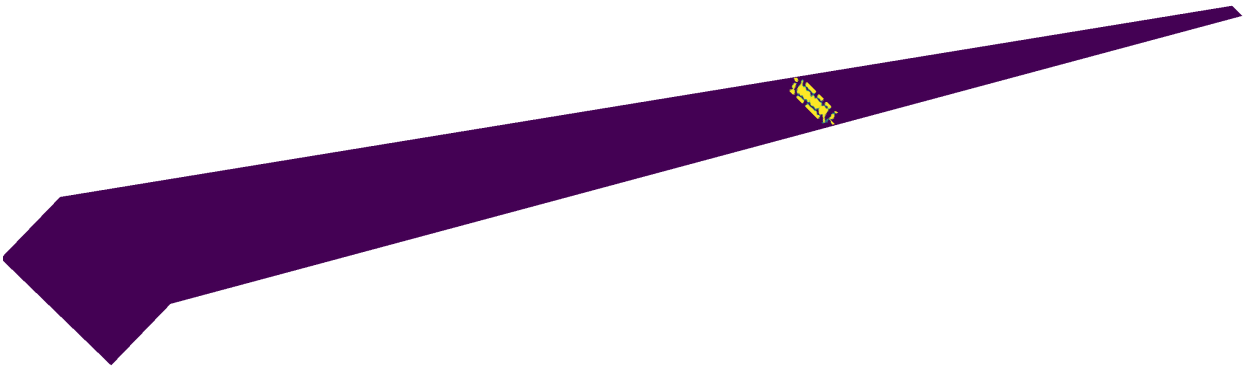

Figure 13: Optimized design of uCRM skin on a wing

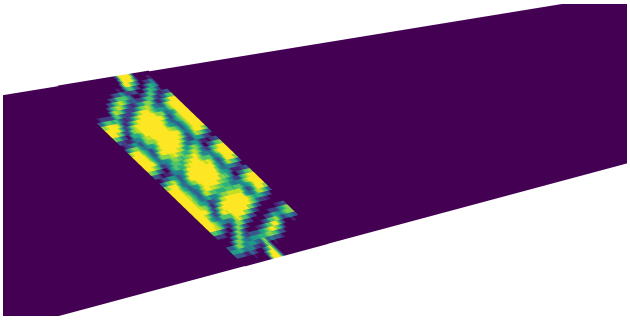

Figure 14: Enlarged view of optimized skin segment

VII. Segment-Wise Topology Optimization

The results from Section VI illustrate the demanding computational requirements needed to obtain an optimized wingbox topology on a full-scale mesh with sufficient resolution to obtain through-thickness structural features. In this section, we present an alternate segment-wise approach which seeks to address these challenges.

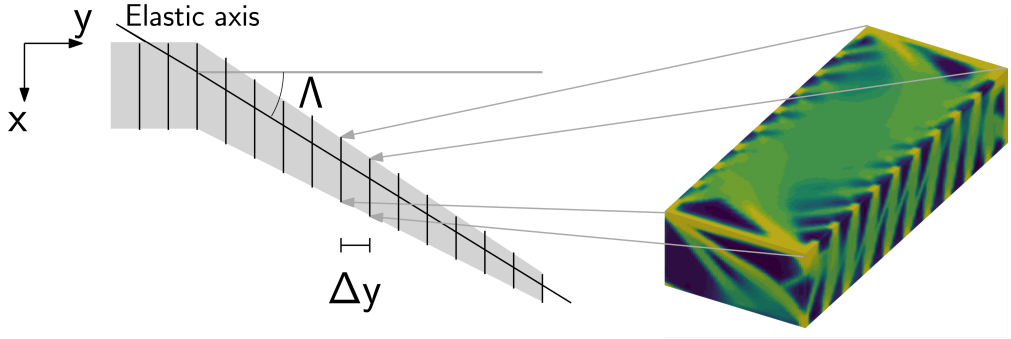

Figure 16: Illustration of Segment-Wise Topology Optimization

Figure 16 illustrates the segment-wise topology optimization approach. In this method, the full-scale wingbox is divided into segments which are optimized independently. As shown in Figure 17, loads on each segment of the wingbox can be estimated independently since the overall wing is statically determinant. This segment-based load determination procedure is illustrated below for an elliptic lift distribution. The extension of this procedure to general, non-elliptic lift distributions poses no difficulty.

The elliptic lift distribution over a wing can be expressed as follows:

$$L'(y) = \frac{\pi}{4} L \sqrt{1 - \left(\frac{2y}{b}\right)^2} \tag{9}$$

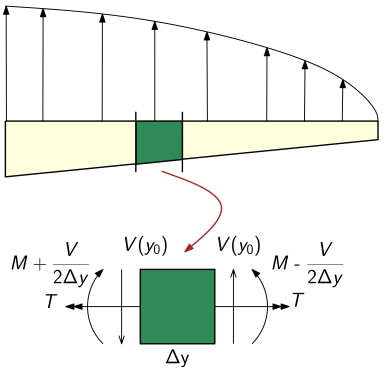

Figure 17: Lift distribution model on uCRM-13.5 wing

where L is the total lift, $L'(y)$ is the lift per unit span, W is the weight of the semi-span of the wing, and $b/2$ is the semi-span. The moment, torque and shear acting at a station y_0 can be determined by integrating the lift distribution as follows:

$$\begin{aligned} M_x(y_0) &= \int_{y_0}^{b/2} (y - y_0) L'(y) dy \\ T_y(y_0) &= \int_{y_0}^{b/2} (y - y_0) \tan(\Lambda) L'(y) dy \\ V_z(y_0) &= \int_{y_0}^{b/2} L'(y) dy \end{aligned} \tag{10}$$

where $M_x(y_0)$, $T_y(y_0)$, and $V_z(y_0)$ are the moment, torque, and shear, respectively, and Λ is the sweep of the wing.

Instead of treating the moment, torque and shear resultants as distributed loads, we impose them as point forces. While the shear loads can be applied directly to the segment, the moment and torque resultants must be resolved into equivalent point forces, as shown in Figure 18. Figure 18 also illustrates the boundary conditions, which are applied to the segment to remove rigid body translation and rotation. Lastly, crushing loads are applied as shown in the figure to simulate the effects of aerodynamic loading.

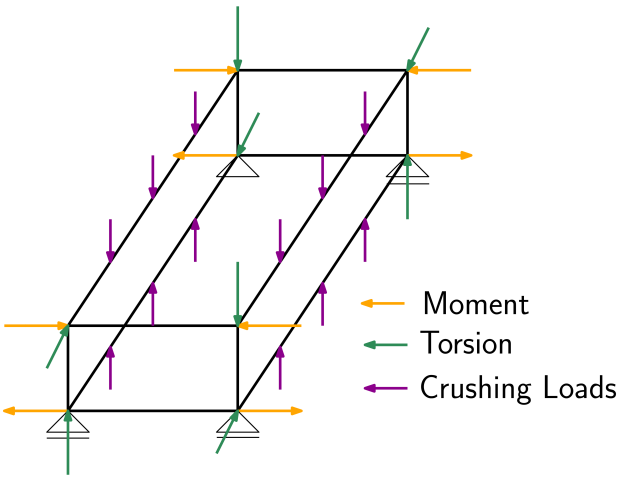

Figure 18: Application of loads to wing segment

Each segment in the wingbox is discretized with 128 chord-wise elements, 64 span-wise elements and 64 through thickness elements, resulting in a mesh with just over 600 000 elements. A single material formulation is used as described above. The compliance-minimization formulation is used based on the prior mass-constrained compliance design formulation (4). Here, we set the mass constraint at 20% of the total solid domain.

The results from the topology optimization of a single segment are shown in Figure 19. The segment-based design method clearly enables better-resolved through thickness structural features with truss-like structure.

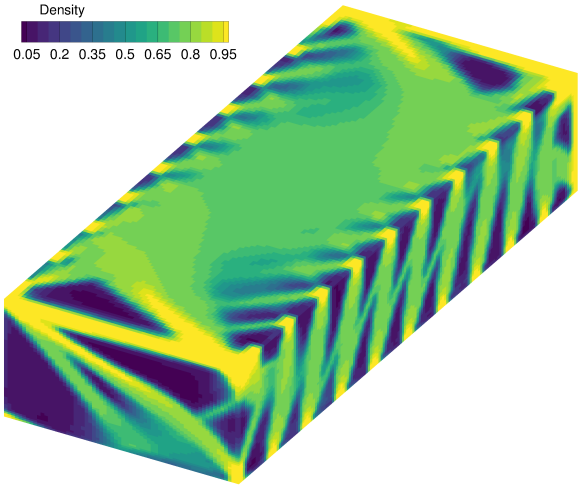

Figure 19: Segment-Wise Optimized Design

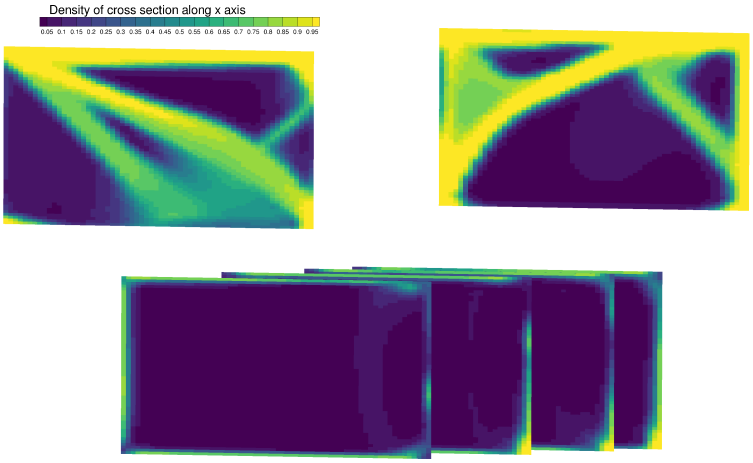

Figure 20: Chord-Wise Optimized Design

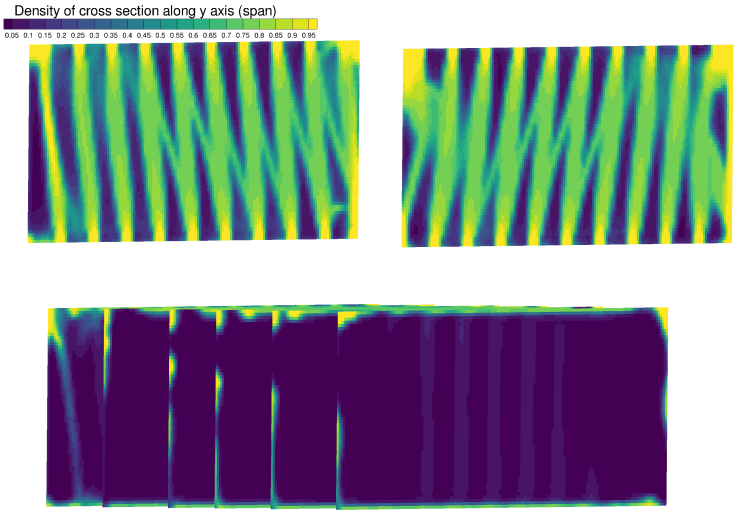

Figure 21: Span-Wise Optimized Design

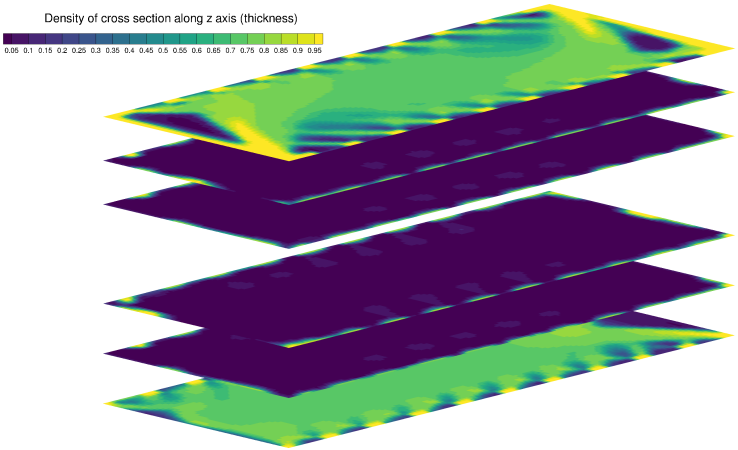

Figure 22: Thickness-Wise Optimized Design

Figures 20, 21 and 22 show the internal structure in the chord-wise, span-wise and through-thickness directions, respectively. The optimized design has material distributed primarily to the surfaces of the wingbox segment, with no internal structure. Figure 20 clearly shows truss-like structures formed at either ends of the segment, while the center remains void in the chord-wise direction. Similarly, Figure 21 shows that the span-wise direction has interesting features at each end of the segment due to the crushing aerodynamic loads. Finally, Figure 22 shows that the optimizer has placed most of the material at the top and bottom surface, forming a skin-like structure for maximum bending stiffness.

VIII. Conclusions

In this paper, we applied large-scale topology optimization techniques to the design of an additively manufactured wingbox structure for the uCRM configuration. Slender, high-aspect ratio aerospace structures place demanding computational requirements on density-based topology optimization methods. To enable the efficient solution of these types of large-scale problems, we presented a parallel analysis and design optimization framework. We applied this framework to mass-constrained compliance minimization of the full-scale uCRM-9 and uCRM-13.5 wingboxes. These full-scale designs exhibited through-thickness intermediate density material, without resolved structural features. Next, we demonstrated the proposed optimization method on buckling-load maximization problems. We found that it was necessary to aggregate more than ten eigenvalues to obtain good panel designs. Finally, we proposed and demonstrated a segment-wise topology optimization technique for wingbox design, which enabled greater through-

thickness resolution of the internal wingbox structure. Results from the segment-based optimization placed most of the solid elements at the extreme surfaces with no intermediate material. Future work will include implementing the segment-wise optimization technique for the design of the entire wing.

References

[1] N. Aage, E. Andreassen, and B. Lazarov. Topology optimization using petsc: An easy-to-use, fully parallel, open source topology optimization framework. *Structural and Multidisciplinary Optimization*, 51(3):565–572, 2015. ISSN 1615-147X. doi:10.1007/s00158-014-1157-0. URL http://dx.doi.org/10.1007/s00158-014-1157-0.

[2] O. Amir, N. Aage, and B. Lazarov. On multigrid-cg for efficient topology optimization. *Structural and Multidisciplinary Optimization*, 49(5):25–57, 2014. ISSN 1615-147X. doi:10.1007/s00158-013-1015-5. URL http://dx.doi.org/10.1007/s00158-013-1015-5.

[3] V. Balabanov and R. Haftka. Topology optimization of transport wing internal structure. *AIAA Journal*, 1994.

[4] M. P. Bendse and N. Kikuchi. Generating optimal topologies in structural design using a homogenization method. *Computer Methods in Applied Mechanics and Engineering*, 71(2):197 – 224, 1988. ISSN 0045-7825. doi:http://dx.doi.org/10.1016/0045-7825(88)90086-2. URL http://www.sciencedirect.com/science/article/pii/0045782588900862.

[5] T. Borrvall and J. Petersson. Large-scale topology optimization in 3d using parallel computing. *Computer Methods in Applied Mechanics and Engineering*, 190(4647):6201 – 6229, 2001. ISSN 0045-7825. doi:http://dx.doi.org/10.1016/S0045-7825(01)00216-X. URL http://www.sciencedirect.com/science/article/pii/S004578250100216X.

[6] T. Bruns and D. Tortorelli. Topology optimization of non-linear elastic structures and compliant mechanisms. *Computer Methods in Applied Mechanics and Engineering*, 190(2627):3443–3459, 2001. ISSN 0045-7825. doi:10.1015/S0045-7825(00)00278-4. URL http://dx.doi.org/10.1015/S0045-7825(00)00278-4.

[7] S. Buchanan. Development of a wingbox rib for a passenger jet aircraft using design optimization and constrained to traditional design and manufacture requirements. In *Altair Technology Conference*, 2007.

[8] P. Dunning, C. J. Brampton, and H. A. Kim. Multidisciplinary level set topology optimization of the internal structure of an aircraft wing. In *Inproceedings of 10th World Congress on Structural and Multidisciplinary Optimization*, San Diego, California, 2013. URL http://www2.mae.ufl.edu/mdo/Papers/5404.pdf.

[9] A. Forsgren, P. E. Gill, and M. H. Wright. Interior methods for nonlinear optimization. *SIAM Review*, 44(4):525–597, 2002. doi:10.1137/S0036144502414942.

[10] X. Gao and H. Ma. Topology optimization of continuum structures under buckling constraints. *Computers & Structures*, 157:142 – 152, 2015. ISSN 0045-7949. doi:http://dx.doi.org/10.1016/j.compstruc.2015.05.020. URL http://www.sciencedirect.com/science/article/pii/S0045794915001662.

[11] S. Grihon, L. Krog, and K. Hertel. A380 weight savings using numerical structural optimization. In *Inproceedings of 20th AAAF Colloqium "Material for Aerospace Application"*, Paris, France, 2004. doi:10.2514/6.2004-4481.

[12] E. Holmberg, B. Torstenfelt, and A. Klarbring. Stress constrained topology optimization. *Structural and Multidisciplinary Optimization*, 48(1):33–47, 2013. ISSN 1615-147X. doi:10.1007/s00158-012-0880-7. URL http://dx.doi.org/10.1007/s00158-012-0880-7.

[13] K. A. James, G. J. Kennedy, and J. R. Martins. Concurrent aerostructural topology optimization of a wing box. *Computers & Structures*, 134(0):1 – 17, 2014. ISSN 0045-7949. URL http://www.sciencedirect.com/science/article/pii/S0045794913003398.

[14] G. J. Kennedy. Strategies for adaptive optimization with aggregation constraints using interior-point methods. *Computers & Structures*, 153(0):217 – 229, 2015. ISSN 0045-7949. doi:10.1016/j.compstruc.2015.02.024.

[15] G. J. Kennedy. Large-scale multimaterial topology optimization for additive manufacturing. In *56th AIAA/ASCE/AHS/ASC Structures, Structural Dynamics, and Materials Conference*, Kissimmee, FL, 2015. URL http://gkennedy.gatech.edu/wp-content/uploads/2015/04/2015_SDM_paper.pdf.

[16] G. J. Kennedy and J. E. Hicken. Improved constraint-aggregation methods. *Computer Methods in Applied Mechanics and Engineering*, 2015. URL http://gkennedy.gatech.edu/wp-content/uploads/2015/03/aggregation_methods.pdf. In press.

[17] G. J. Kennedy and J. R. R. A. Martins. A parallel finite-element framework for large-scale gradient-based design optimization of high-performance structures. *Finite Elements in Analysis and Design*, 87(0):56 – 73, 2014. ISSN 0168-874X. URL http://gkennedy.gatech.edu/wp-content/uploads/2014/12/2013_tacs_paper.pdf.

[18] G. J. Kennedy and J. R. R. A. Martins. A parallel aerostructural optimization framework for aircraft design studies. *Structural and Multidisciplinary Optimization*, pages 1–23, 2014. ISSN 1615-147X. URL http://gkennedy.gatech.edu/wp-content/uploads/2014/12/2013_tripan_paper.pdf.

[19] G. K. W. Kenway, G. J. Kennedy, and J. R. R. A. Martins. Aerostructural optimization of the Common Research Model configuration. In *15th AIAA/ISSMO Multidisciplinary Analysis and Optimization Conference*, Atlanta, GA, June 2014. AIAA 2014-3274 (Best Paper Award).

[20] L. Krog, A. Tucker, M. Kemp, and R. Boyd. Toplogy optimization of wing box ribs. In *10th AIAA/ISSMO Multidisciplinary Analysis and Optimization Conference*, Albany, New York, 2004.

[21] E. Lindgaard and J. Dahl. On compliance and buckling objective functions in topology optimization of snap-through problems. *Structural and Multidisciplinary Optimization*, 47(3):409–421, 2013. ISSN 1615-147X. doi:10.1007/s00158-012-0832-2. URL http://dx.doi.org/10.1007/s00158-012-0832-2.

[22] K. Maute and M. Allen. Conceptual design of aeroelastic structures by topology optimization. *Structural and Multidisciplinary Optimization*, 27(1-2):27–42, 2004. ISSN 1615-147X. doi:10.1007/s00158-003-0362-z. URL http://dx.doi.org/10.1007/s00158-003-0362-z.

[23] M. Neves, H. Rodrigues, and J. Guedes. Generalized topology design of structures with a buckling load criterion. *Structural optimization*, 10(2):71–78, 1995. ISSN 0934-4373. doi:10.1007/BF01743533. URL http://dx.doi.org/10.1007/BF01743533.

[24] N. Olhoff. Multicriterion structural optimization via bound formulation and mathematical programming. *Structural and Multidisciplinary Optimization*, 1:11–17, 1989. ISSN 1615-147X. doi:10.1007/BF01743805.

[25] Y. Saad. A flexible inner-outer preconditioned gmres algorithm. *SIAM Journal on Scientific Computing*, 14(2):461–469, 1993. doi:10.1137/0914028.

[26] Y. Saad. *Iterative Methods for Sparse Linear Systems*. SIAM, 2nd edition, 2003.

[27] Y. Saad and M. H. Schultz. GMRES: A generalized minimal residual algorithm for solving nonsymmetric linear systems. *SIAM Journal on Scientific and Statistical Computing*, 7(3):856–869, 1986. doi:10.1137/0907058.

[28] A. P. Seyranian, E. Lund, and N. Olhoff. Multiple eigenvalues in structural optimization problems. *Structural and Multidisciplinary Optimization*, 8:207–227, 1994. ISSN 1615-147X. doi:10.1007/BF01742705.

[29] O. Sigmund and J. Petersson. Numerical instabilities in topology optimization: A survey on procedures dealing with checkerboards, mesh-dependencies and local minima. *Structural optimization*, 16(1):68–75, 1998. ISSN 0934-4373. doi:10.1007/BF01214002. URL http://dx.doi.org/10.1007/BF01214002.

[30] M. Stople and K. Svanberg. An alternative interpolation scheme for minimum compliance topology optimization. *Structural and Multidisciplinary Optimization*, 22:116–124, 2001. ISSN 1615-147X. doi:10.1007/s001580100129.

[31] J. Taylor and M. P. Bendsøe. An interpretation for min-max structural design problems including a method for relaxing constraints. *International Journal of Solids and Structures*, 20(4):301 – 314, 1984. ISSN 0020-7683. doi:http://dx.doi.org/10.1016/0020-7683(84)90041-6. URL http://www.sciencedirect.com/science/article/pii/0020768384900416.

[32] J. C. Vassberg, M. A. DeHaan, S. M. Rivers, and R. A. Wahls. Development of a common research model for applied CFD validation studies. 2008. AIAA 2008-6919.

[33] A. Verbart, M. Langelaar, N. Van Dijk, and F. Van Keulen. Level set based topology optimization with stress constraints and consistent sensitivity analysis. In *53rd AIAA/ASME/ASCE/AHS/ASC Structures, Structural Dynamics and Materials Conference 20th AIAA/ASME/AHS Adaptive Structures Conference 14th AIAA*, page 1358, 2012.

[34] A. Wächter and L. T. Biegler. On the implementation of an interior-point filter line-search algorithm for large-scale nonlinear programming. *Mathematical Programming*, 106(1):25–57, 2006. ISSN 0025-5610. doi:10.1007/s10107-004-0559-y. URL http://dx.doi.org/10.1007/s10107-004-0559-y.

[35] P. Wesseling. *An introduction to multigrid methods*. John Wiley & Sons, 1992.